




Article

Buried Interface Smoothing Boosts the Mechanical Durability and Efficiency of Flexible Perovskite Solar Cells

Erxin Zhao ^{1,†}, Yongshuai Gong ^{2,†} , Yixin Dong ², Wanlei Dai ³, Chou Liu ¹, Tinghuan Yang ¹ , Nan Wu ¹, Ye Yang ¹, Zheng Zhang ¹, Chenqing Tian ¹, Buyi Yan ³, Dongxue Liu ^{2,*}, Lu Zhang ^{3,*} and Tianqi Niu ^{1,*} 

¹ Key Laboratory of Applied Surface and Colloid Chemistry, National Ministry of Education, Shaanxi Key Laboratory for Advanced Energy Devices, Shaanxi Engineering Lab for Advanced Energy Technology, School of Materials Science and Engineering, Shaanxi Normal University, Xi'an 710119, China; erxinzhao@snnu.edu.cn (E.Z.); carlliu19@outlook.com (C.L.); th_yang@snnu.edu.cn (T.Y.); wunan@snnu.edu.cn (N.W.); yeyang@snnu.edu.cn (Y.Y.); lzhengzhang@snnu.edu.cn (Z.Z.); chenqing_tian@snnu.edu.cn (C.T.)

² Three Gorges Corporation, Science and Technology Research Institute, Beijing 101199, China; gong_yongshuai@ctg.com.cn (Y.G.); dong_yixin@ctg.com.cn (Y.D.)

³ Microquanta Semiconductor Co., Ltd., Hangzhou 310027, China; wanlei.d01@microquanta.com (W.D.)

* Correspondence: liu_dongxue@ctg.com.cn (D.L.); l.zhang01@microquanta.com (L.Z.); niutq@snnu.edu.cn (T.N.)

† These authors contributed equally to this work.

Abstract: Flexible perovskite solar cells (F-PSCs) have the advantages of high power-per-weight, solution processability, and bending durability and have emerged as a competitive photovoltaic technology for various applications. As the core electron transport layer (ETL) in n-i-p-type device configurations, the solution-processed SnO₂ generally suffers from serious defect stacking on films, compromising the charge transport properties and the performance of resulting devices. Herein, we proposed a media-filling strategy to optimize the contact quality at the buried interface by introducing Al₂O₃ nanoparticles on the SnO₂ surface. Rather than forming a compact insulating layer, the Al₂O₃ can fill the grain boundaries of SnO₂ and smooth the substrate surface. Optimized interfacial contact under careful concentration control can rationally minimize the contact area of the perovskite with the surface imperfections of SnO₂ to mitigate trap-assisted charge recombination. Furthermore, the reduced surface roughness of SnO₂ facilitates the uniform deposition and oriented growth of upper perovskite film. As a result, the target F-PSCs achieved an impressive efficiency of 23.83% and retained 80% of the initial performance after 5000 bending cycles at a radius of four mm.

Keywords: interfacial contact; electron extraction; Al₂O₃; flexible; perovskite solar cells



Academic Editor: Francesco Calise

Received: 5 December 2024

Revised: 21 December 2024

Accepted: 28 December 2024

Published: 3 January 2025

Citation: Zhao, E.; Gong, Y.; Dong, Y.; Dai, W.; Liu, C.; Yang, T.; Wu, N.; Yang, Y.; Zhang, Z.; Tian, C.; et al. Buried Interface Smoothing Boosts the Mechanical Durability and Efficiency of Flexible Perovskite Solar Cells.

Energies **2025**, *18*, 174. <https://doi.org/10.3390/en18010174>

Copyright: © 2024 by the authors. Licensee MDPI, Basel, Switzerland. This article is an open access article distributed under the terms and conditions of the Creative Commons Attribution (CC BY) license (<https://creativecommons.org/licenses/by/4.0/>).

1. Introduction

Flexible perovskite solar cells (F-PSCs) have demonstrated significant advantages, such as high power-per-weight ratios, flexibility [1,2], and compatibility for large-scale preparations by solution processing and have attracted tremendous academic and commercial attention [3–5]. These advantageous features position them as a promising candidate [6,7] to supply constant energy for wearable electronic devices within the evolving landscape of the Internet of Things (IoTs) [8–10]. Benefiting from the exceptional optoelectronic properties of metal halide perovskite, F-PSCs have delivered a rapid increase in power conversion efficiency (PCE) of over 25% to date [11]. However, the current record efficiency of F-PSCs remains inferior to that of their rigid counterparts. The practicality of this lightweight

photovoltaic technology has also been restrained by their compromised mechanical stability over long-term bending cycles [12]. These limitations are primarily attributed to the intricate low-temperature procedure [13] and inhomogeneity of flexible substrates, which raises the difficulty for the high-quality deposition of the subsequent functional layers in devices [10,14]. The rough contact interface between the charge transport layer and perovskite film can deteriorate the weak interfacial adhesion, thus resulting in problems with mechanical delamination and the bending fragility of F-PSCs [15]. Moreover, the significant energy loss at the buried interface has emerged as the dominant hindrance that limits the further development of F-PSCs.

Due to its high electron mobility, good optical transmittance, and chemical stability, SnO₂ has emerged as a promising electron transport layer for F-PSCs. However, the solution-processed SnO₂ layer using colloidal dispersion generally suffers from numerous Sn dangling bonds and hydroxyl groups on the resulting film surface. These active sites can absorb O₂ and H₂O from the environment, facilitating electron capture and elevating the charge transport barrier [16]. Furthermore, the presence of voids and surface imperfections in SnO₂ film may compromise the crystal growth and morphology quality of upper perovskite films, consequently affecting the overall performance of devices. To optimize the buried interface of F-PSCs, previous researchers have predominantly concentrated on molecular modification to tailor interfacial properties [17]. The functional molecules can passivate the surface traps through chemical coordination or ionic bonding, facilitating improved interface contact and enhanced charge transport kinetics in F-PSCs. However, organic molecular modification is generally limited by the bonding effect, which is inadequate for the efficient suppression of interfacial imperfections. An increased incorporation concentration would reversely deteriorate the charge transport due to the increased series resistance. Therefore, molecular modification largely relies on a tedious trial-and-error process, which inevitably increases the preparation cost and deteriorates the device reproductivity. Additionally, the high roughness of flexible substrates further threatens the compactness and conformal alignment of SnO₂ colloids, particularly affecting high-throughput and scalable fabrications. As such, the surface imperfections of SnO₂ pose a decisive risk to the structural integrity and functionality of F-PSCs, highlighting the importance of rational interfacial modulation in the deposition process [18].

Alternatively, incorporating metal-oxide nanoparticles has been confirmed to have an effect on optimizing SnO₂ film. For example, Cheng et al. constructed a SnO₂/TiO₂ bilayer by spin-coating the TiO₂ nanoparticles on the SnO₂ ETL, resulting in the formation of cascade-aligned energy levels and reducing the energetic barrier for electron transfer [19]. In contrast to utilizing n-type semiconductors with a high electron conductivity in a bilayered structure, some insulating metal oxides such as Al₂O₃ and MgO were employed to modify the SnO₂ layer by smoothing substrates. For example, Brown et al. introduced the MgO on the top of SnO₂ ETL to boost the rectification ratio, reduce interfacial recombination, and improve the shelf-life stability of PSCs. Xu et al. deposited AlO_x via atomic layer deposition (ALD) as a buffer layer on an ITO substrate to promote the dense and conformal coating of SnO₂ nanoparticles and improve electron extraction at the cathode interface [20]. Despite these advances, the feasibility of using wide-bandgap metal oxidates as the buffer layer or interfacial filler for the F-PSCs has rarely been reported. The influences of media filing on the interfacial properties of SnO₂ and upper perovskite layers are still being explored. Thus, developing a controllable optimization strategy for the buried interface is imperative to optimize the charge transfer and boost the efficiency and mechanical robustness of F-PSCs.

In this study, we proposed an interfacial smoothing strategy for the buried contact of F-PSCs by introducing porous Al₂O₃ nanoparticles at the SnO₂-perovskite interface. In contrast to traditional molecular passivation, the Al₂O₃ nanoparticles can improve the

carrier kinetics of F-PSCs by reducing the contact area of the perovskite layer with the defective substrates while maintaining the necessary electron extraction channels. Rather than forming a dense insulating layer on the SnO₂ surface, the Al₂O₃ nanoparticles were inserted into the grain boundaries of polycrystalline SnO₂ and created randomly distributed nanoscale openings. This optimized distribution of Al₂O₃ can largely avoid the thickness-dependent electron tunneling from compact stacking, mitigate the impacts of surface imperfections on the charge transport, and suppress trap-induced non-radiative loss at the cathode interface. Simultaneously, the surface-filling effect of Al₂O₃ nanoparticles can improve the uniformity and roughness of the SnO₂ layer, which subsequently facilitates high-quality perovskite deposition featuring enhanced crystallinity and well-connected grain stacking. The synergistic optimization of the buried interface by the addition of Al₂O₃ contributed to efficient charge transport with significantly suppressed energy loss in devices. Finally, the target F-PSCs achieved the optimal efficiency of 23.83%, outperforming the control device, which had an efficiency of 20.98%. The Al₂O₃ decoration also improved the humidity resistance and mechanical stability of F-PSCs, which retained over 80% of the initial performance after ambient aging for 30 days or 5000 bending cycles at a radius of 4 mm. This work provides inspiration for buried interface modulation beyond molecular modification for high-performance F-PSCs, which may increase the broad applicability of physical contact optimization for the large-scale production of F-PSCs.

2. Materials and Methods

2.1. Materials

Formamidinium iodide (FAI), lead iodide (PbI₂), Spiro-OMeTAD powder, and methylamine hydrochloride (MACl) were purchased from Advanced Election Technology Co., Ltd., Shenyang, Liaoning, China, Methylammonium iodide (MAI), cesium iodide (CsI), and 2-Phenylethanamine hydroiodide (PEAI) were purchased from Xi'an Yuri Solar Co., Ltd., Xi'an, China. Dimethylsulfoxide (DMSO) and N,N-dimethylformamide (DMF) were purchased from Aladdin. 4-tert-butylpyridine (TBP), Li-bis-(trifluoromethanesulfonyl) imide (Li-TFSI), tin(IV) oxide (SnO₂), colloidal dispersion liquid (15% in H₂O), and aluminum oxide ethanol dispersion (Al₂O₃, particle size of ca. 100 nm) were purchased from Alfa Aesar, Ward Hill, MA, USA. Isopropanol (IPA) was purchased from Sinopharm Chemical Reagent Co., Ltd., Beijing, China. Chlorobenzene (CB) and ethanol anhydrous (Et(OH)₂) were purchased from Sigma-Aldrich, Shanghai, China. All chemicals and solvents were used directly as received.

2.2. Preparation of Perovskite Precursor Solution

The perovskite solution was prepared by dissolving 645 mg PbI₂, 221 mg FAI, 15 mg CsI, 9 mg MAI, and 38 mg MACl in 1 mL mixed solvent of DMF and DMSO (volume ratio of 4:1). The solution was stirred for 12 h and then filtered by 0.22 μm syringe filter for later use.

2.3. Fabrication of F-PSCs

The flexible substrate was cleaned and adhered to the rigid soda-lime glass using PDMS, securing the ends with tape and leaving an area for the electrodes. The clean flexible substrate polyethylene terephthalate/indium tin oxide (PET/ITO) was treated with UV–ozone for 16 min. SnO₂ was dissolved in ultrapure water at a ratio of 1:6 and stirred for 2 h before its use. After the PET/ITO cooled down, 150 μL of SnO₂ colloidal solution was spin-coated on PET/ITO at 4000 rpm for 30 s and then annealed at 100 °C for 30 min after spin coating. Isopropanol was used to dilute the aluminum oxide ethanol dispersion to different concentrations (volume ratios of 1:2, 1:4 and 1:6), and the mixture was stirred

for 2 h. The Al₂O₃ ethanol dispersion (150 µL) was spin-coated on the SnO₂ substrate at 3000 rpm for 30 s and then annealed in air at 100 °C for 10 min. Before spin coating, SnO₂ ETL was treated with UV–ozone for 12 min. The perovskite film was prepared by a one-step spin-coating procedure at 6000 rpm for 30 s. Twenty s before the end of the process, 130 µL antisolvent (chlorobenzene) was dropped onto the substrates, which were then annealed at 120 °C (under the following conditions: ~25 °C temperature; ~5% humidity) for 30 min. 2-Phenylethanamine hydroiodide (PEAI) was dissolved in isopropyl alcohol and stirred for 4 h. PEAH was coated with 3000 rpm for 30 s. Then the hole transport layer (HTL) was fabricated by spin coating 45 µL of Spiro-OMeTAD solution (90 mg Spiro-OMeTAD, 22 µL of Li-TFSI, and 36 µL TBP in 1 mL CB). The 80 nm Au electrode was deposited on the HTL.

2.4. Device Characterizations

Scanning electron microscope (SEM) images were acquired using field-emission SEM (SU8020, Hitachi, Tokyo, Japan). The AFM images were acquired using an atomic force microscope (Dimension Icon, BRUKER, Billerica, MA, USA). X-ray diffraction (XRD) patterns were recorded on a X-ray diffractometer (Smart Lab, Rigaku, Japan). UV-vis absorption spectra were obtained by a UV-vis spectrophotometer (PerkinElmer UV-Lambda 950, Waltham, MA, USA). Steady-state photoluminescence (PL) and time-resolved photoluminescence (TRPL) spectra were measured on a fluorescence spectrometer (PicoQuant FT-300, Berlin, Germany). The current density–voltage (*J*-*V*) curves were obtained in the air with a Keithley 2400 source meter under the AM 1.5 radiation condition (100 mW/cm²). The scan range was from 1.5 to 0 V with a 0.02 V bias step. The external quantum efficiency (EQE) measurements were conducted under a 300 W Xenon lamp light source with a QTest Station 2000ADI system (Enli Technology Co., Ltd., Taipei, Taiwan, China), with the monochromatic light intensity calibrated by a reference silicon photodiode. The EIS and C-*V* measurements were performed using a Zahner Zennium electrochemical workstation.

3. Results and Discussion

3.1. Interfacial Morphology and Electrical Properties of SnO₂

We first conducted atomic force microscopy (AFM) to evaluate the surface topography of the SnO₂ films. As shown in Figure 1a, the average roughness (*R*_a) of the pristine SnO₂ films was determined to be 19 nm, indicating the rough surface of the SnO₂ nanocrystals on the surface under solution processing. Then, we deposited the perovskite film onto the SnO₂ substrate, which was exfoliated from the substrate to expose the bottom interface [21]. The morphology of the buried interface was examined using scanning electron microscopy (SEM), illustrating a high density of pinholes on the bottom of the perovskite films, indicating the poor interface adhesion at the perovskite-SnO₂ interface (Figure 1b). The existence of holes could be attributed to the poor uniformity and flatness of the SnO₂ substrate, leading to the elevated difference in the surface energy across the different areas (Figure 1c). The subsequent perovskite deposition onto the irregular substrate can disturb the nucleation sites and intensify the randomness in the growth orientation of perovskite crystals. The lattice extrusion at the bottom surface causes the crystal deformation, thereby deteriorating the film quality.

After introducing Al₂O₃ nanoparticles on the SnO₂ surface, we noted a reduction in *R*_a from 19 to 16 nm, as demonstrated by the AFM results (Figure 1d). This indicates the Al₂O₃ nanoparticles could fill the grooves on the SnO₂ film, thereby reducing its roughness. The SEM images of the perovskite film on the SnO₂/Al₂O₃ substrate showed the densely packed grains at the buried interface with no obvious void residue (Figure 1e). Collectively, the enhancement in surface quality of SnO₂ could facilitate the high-quality deposition of

perovskite films, potentially improving the interfacial contact and carrier transport kinetics (Figure 1f).

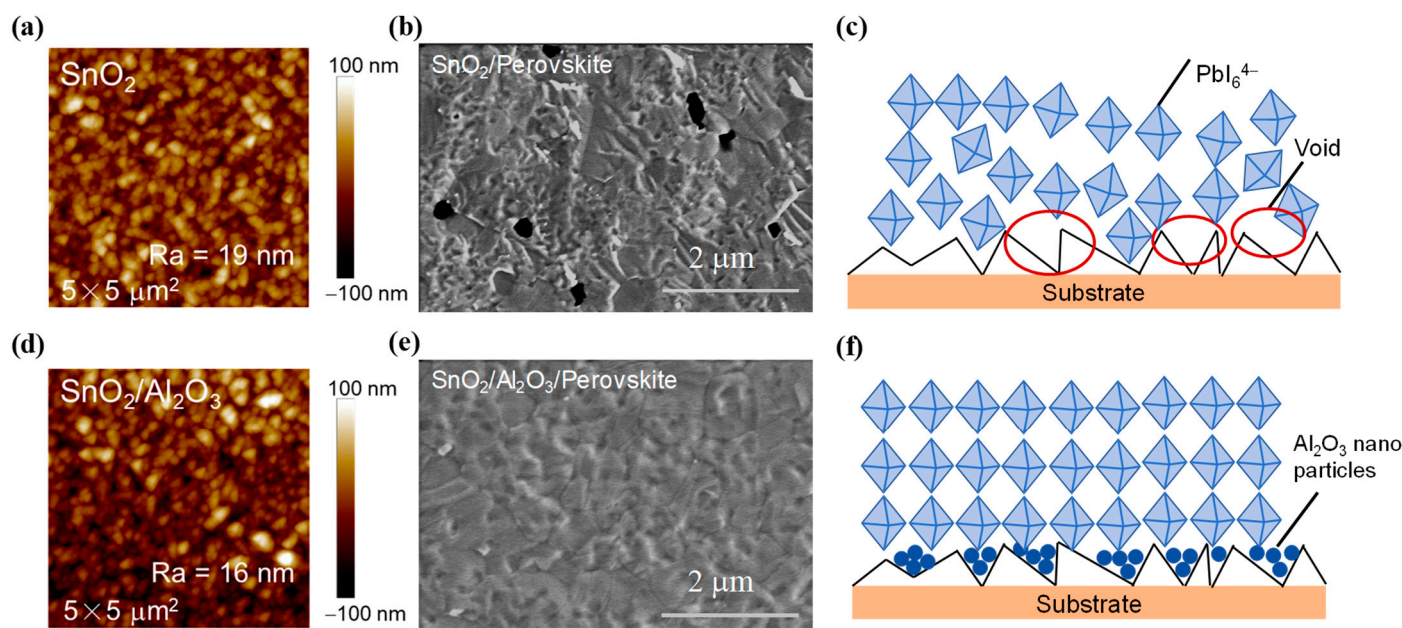


Figure 1. (a,d) AFM topography of pristine SnO₂ and SnO₂/Al₂O₃ films. (b,e) SEM images of buried interface of perovskite films deposited on SnO₂ and SnO₂/Al₂O₃. Schematic illustration showing crystal stacking modes of perovskite on the (c) SnO₂ and (f) SnO₂/Al₂O₃ substrates.

To explore the effect of Al₂O₃ modification on SnO₂ films, X-ray diffraction (XRD) was performed to assess the crystalline quality of SnO₂ ETL films before and after the addition of Al₂O₃. Figure 2a shows that introducing Al₂O₃ nanoparticles results in negligible variation in the crystal stacking structure of SnO₂ films. Similarly, the optical bandgap of different SnO₂ films retains the same value of 4.02 eV (Figure S1). Figure 2b shows the optical transmittance spectra of the SnO₂ substrates in the 300–900 nm region, illustrating the uncompromised transmittance of SnO₂ with the introduction of Al₂O₃ nanoparticles. The high light transmittance of bottom substrates ensures the adequate optical absorption of upper perovskite films. In addition, based on the space charge limited current (SCLC) method, the electron-only device structure of ITO/SnO₂/Ag was fabricated to assess the electrical properties of the ETL substrates (Figure S2). The electron mobility was calculated by the Mott–Gurney formula [22]:

$$J_D = 9\mu\epsilon\epsilon_0 V^2 / 8L^3 \quad (1)$$

where ϵ is the relative dielectric constant, ϵ_0 is the vacuum dielectric constant, and L is the film thickness. Compared to pure SnO₂, the electron mobility of SnO₂ films modified with Al₂O₃ was increased from 6.53×10^{-3} to 11.7×10^{-3} cm² V⁻¹ S⁻¹ (Figure 2c), indicating the enhanced carrier transport capacity of SnO₂/Al₂O₃ film. The conductivity of ETLs was further tested, which can be calculated by the following formula:

$$I = \sigma A d^{-1} \quad (2)$$

where A is the device area and d represents the thickness of SnO₂ ETL [23]. According to the current–voltage (I - V) curves shown in Figure 2d, the Al₂O₃-modified SnO₂ showed increased conductivity from 2.27×10^{-3} to 4.21×10^{-3} cm² V⁻¹ S⁻¹ compared to the pris-

tine SnO₂. These findings suggest that modification with Al₂O₃ nanoparticles is an efficient approach to improve the electron transport properties of ETLs on flexible substrates.

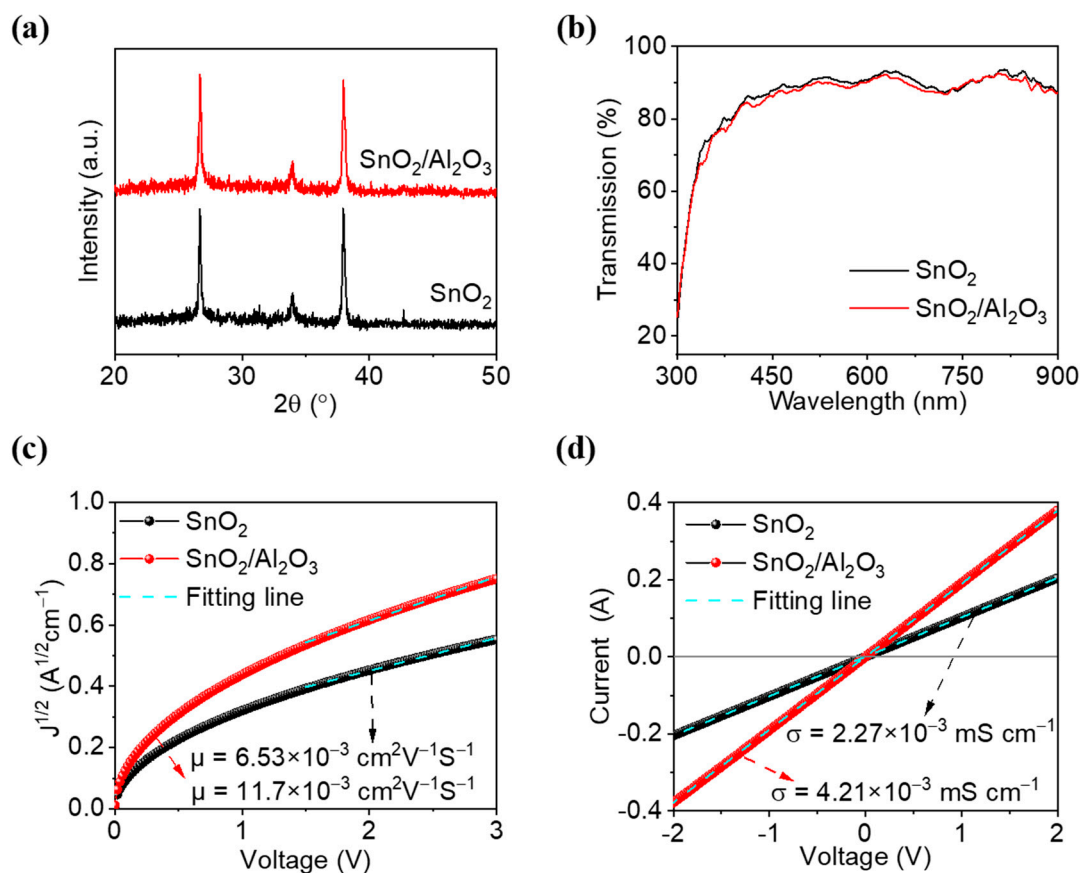


Figure 2. (a) XRD patterns, (b) optical transmittance spectra, (c) electron mobility, and (d) conductivity tests of the SnO₂ films with and without Al₂O₃ decoration.

3.2. Morphology and Crystallinity of Flexible Perovskite Films

SEM and AFM measurements were employed to further evaluate the film formation quality of perovskite on SnO₂ and SnO₂/Al₂O₃ substrates, referred to as the control and target in the following discussion, respectively. As shown in Figure 3a,b, the target film exhibits a lower surface roughness than the control film (18 vs. 33 nm). This reduction in film roughness could be attributed to the flattening effect of the Al₂O₃ filling at the SnO₂ grooves. Moreover, the target film shows fewer grain boundaries and larger grain sizes, with the average grain size increasing from 0.5 to 1.1 μm (Figure 3c–f). These observations indicate that the Al₂O₃ nanoparticles can support a smooth interface condition for the uniform nucleation growth of perovskite crystals, thereby enhancing the crystalline quality of perovskite films. Figure 3g presents the XRD patterns of the perovskite films. Diffraction peaks at 13.94° and 28.08° were detected in the control and target films, corresponding to the (100) and (200) crystal planes, respectively. Notably, the films deposited on the Al₂O₃-modified substrate exhibit a stronger XRD diffraction intensity and a narrower half-peak width (FWHM) for the (100) crystal plane, as shown in Figure 3h. This indicates that the crystallinity of the films is significantly enhanced, which is mainly attributed to the improvement of film crystallization by the flattening filling strategy for Al₂O₃ nanoparticles. The above results indicate that the flattening of ETL layers can effectively promote high-quality crystallization and the growth of the perovskite films and can maintain similar absorption band edges (Figure 3i). Figure S3 shows that the bandgap of the control and target perovskite films is 1.55 eV.

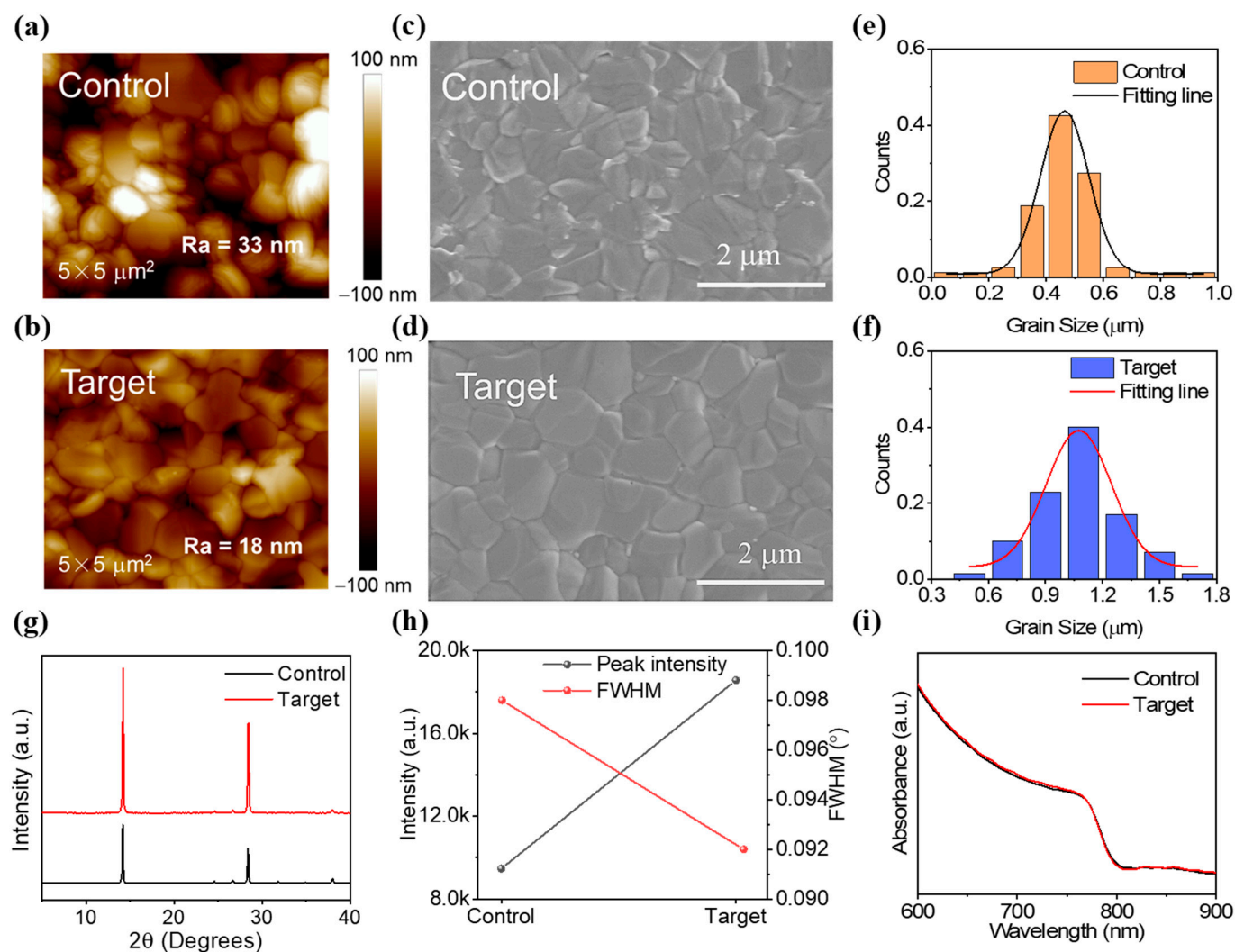


Figure 3. (a,b) AFM topography of (a) control and (b) target perovskite films, showing the average root-mean-square roughness (Ra). (c,d) Top-view SEM images of control and target films. (e,f) Statistical diagram of grain-size distribution of perovskite films. (g) XRD patterns of perovskite films. (h) Peak intensity and FWHM of the (100) plane of perovskite. (i) UV-vis absorption spectra.

3.3. Optical and Electrical Properties of Flexible Perovskite Film

We further explored the effect of Al₂O₃-modified SnO₂ on the optoelectrical properties of the films using steady-state photoluminescence (PL) and time-resolved photoluminescence (TRPL) characterizations. As shown in Figure 4a, the PL peaks for both the control and target films are around 780 nm, with no distinct shift observed. In contrast, the peak intensity of the target film is notably reduced, suggesting that the modified SnO₂ ETL has a higher charge extraction capacity than the control. The PL mapping further demonstrated faster charge extraction and a uniform film morphology in the target case, facilitating the suppressed non-radiative recombination loss at the buried interface (Figure 4b) [24]. TRPL spectra were further examined to determine the carrier kinetics, as illustrated in Figure 4c. The carrier lifetime was determined using the following double exponential function:

$$\tau(t) = A_1 \exp(-t/\tau_1) + A_2 \exp(-t/\tau_2) + B \quad (3)$$

where A_1 and A_2 are the corresponding decay amplitudes, τ_1 and τ_2 are the slow and fast decay time constants, respectively, and B is a constant [25]. For the SnO₂/perovskite case, the fast decay process (τ_1) is driven by interfacial charge transfer, while the slow

decay process (τ_2) is associated with the radiative recombination of free carriers within the bulk perovskite layers. For the fitting parameters listed in Table S1, the τ_1 was decreased from 47.4 to 9.5 ns and the τ_2 was reduced from 246.3 to 142.1 ns with the incorporation of the Al_2O_3 nanoparticles. The average carrier lifetimes of the control and target films were calculated to be 234.3 and 133.5 ns, respectively. The decreased carrier lifetime in the target film confirms that the Al_2O_3 -modified buried interface delivers an improved charge extraction capability.

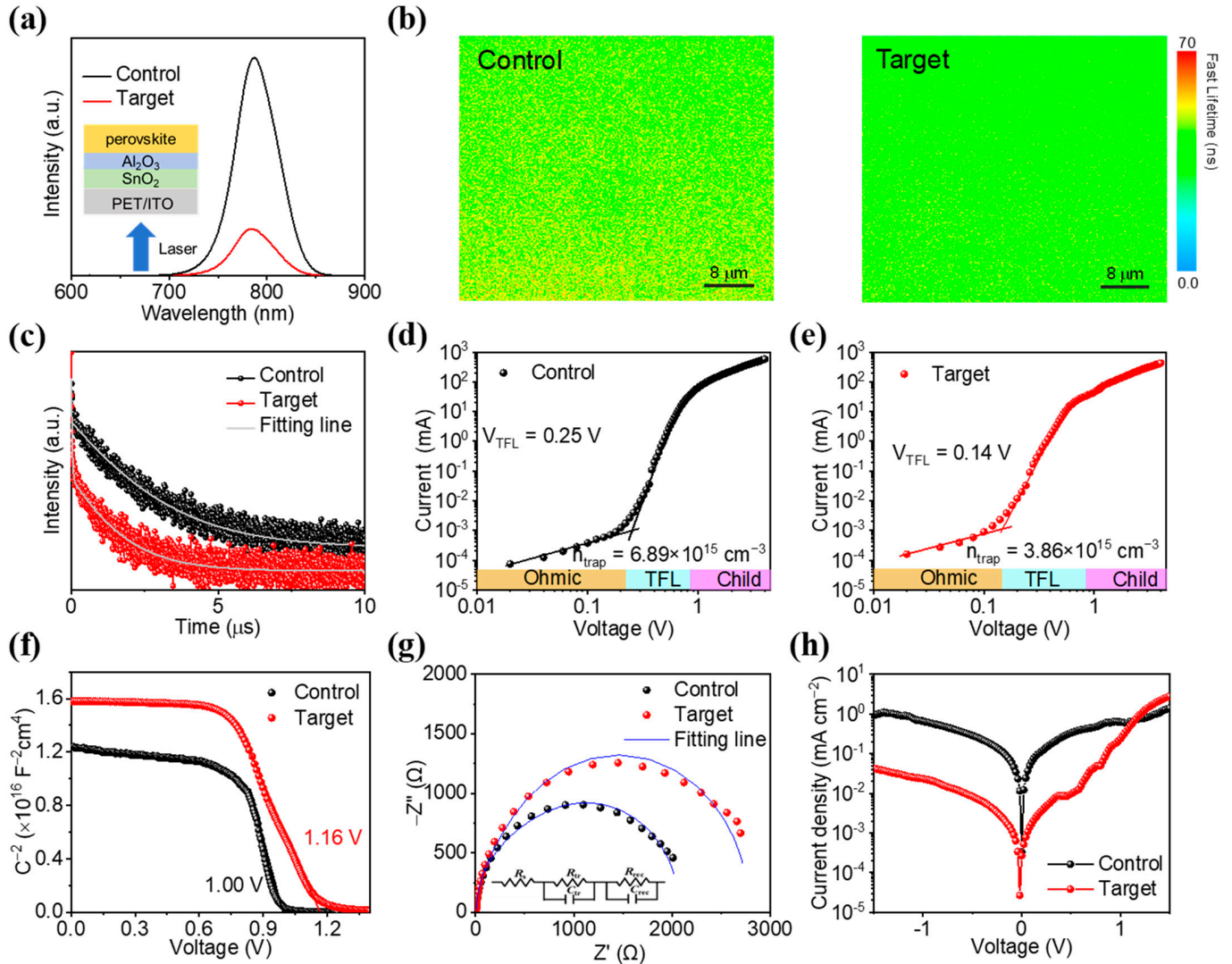


Figure 4. (a) Steady-state PL spectra, (b) PL lifetime in mapping images, (c) TRPL spectra for control and target perovskite films, dark I - V measurement of the electron-only device for (d) the control and (e) the target cases. (f) Mott–Schottky curves, (g) EIS measurement, (h) dark J - V characteristics of control and target devices.

In order to further evaluate the defects density within perovskite films deposited on different substrates, we tested the dark current–voltage curves (I - V) of the devices with the structure of ITO/SnO₂/perovskite/PCBM/Ag via the SCLC method. The trap density was determined by the following formula [26]:

$$n_{\text{trap}} = \frac{2\varepsilon_0\varepsilon_r V_{\text{TFL}}}{eL^2} \quad (4)$$

where ε_r is the relative dielectric constant of perovskite ($\varepsilon_r = 62.3$), V_{TFL} is the starting voltage of the limit region of defect filling, e is the amount of electron charge ($e = 1.6 \times 10^{-19}$ C),

and L is the thickness of perovskite film. As shown in Figure 4d,e, the defect density of the device was reduced from 6.89×10^{15} to $3.86 \times 10^{15} \text{ cm}^{-3}$ after the modification with Al_2O_3 nanoparticles. Additionally, a Mott–Schottky analysis was applied to evaluate the built-in electric field (V_{bi}) of the devices [27]. As shown in Figure 4f, the Al_2O_3 -modified device exhibits a higher V_{bi} compared to the control device, with values increasing from 1.08 to 1.16 V. This indicates that the modified device has a stronger driving force for charge transport, which could contribute to the improved carrier kinetics at the buried interface and the improvement in the V_{OC} of the device [28]. Figure 4g presents the electrochemical impedance spectra (EIS) of the devices. According to the fitting results in Table S2, the modified device shows a smaller transport resistance (R_{tr}) and a larger recombination resistance (R_{rec}) than the control after introducing Al_2O_3 nanoparticles, indicating suppressed trap-induced recombination [29]. The dark J - V curves further illustrate the lower leakage current of the target device concerning the control case, implying the blocking effect of Al_2O_3 nanoparticles on the carrier drift to the ETLs. Collecting the findings above, the Al_2O_3 modification can reduce the contact area of the perovskite under defect-enriched interface conditions and supplement a smoother film surface for carrier transport. These benefits effectively accelerate carrier extraction and alleviate the non-radiative recombination loss at the cathode layer, ensuring enhancements in device performance [30].

3.4. Flexible Solar Cells and Device Stability

Based on the SnO_2 smoothing strategy, we fabricated the n-i-p F-PSCs with the device configuration of ITO/ SnO_2 / Al_2O_3 /perovskite/Spiro-OMeTAD/Au (Figure S4). We first evaluated the influence of the incorporation concentration of trace amounts of Al_2O_3 on the device performance. The corresponding J - V curves of the devices are illustrated in Figure 5a, and detailed parameters are summarized in Table S3. The control device showed a PCE of 20.98%, with a V_{OC} of 1.10 V, a J_{SC} of 24.58 mA cm^{-2} , and an FF of 77.58%. As the concentration of Al_2O_3 nanoparticles increased, the PCE of modified devices showed an increasing trend to reach a maximum at a concentration of 1:4 and declined at higher concentrations. The excessive incorporation concentration of Al_2O_3 nanoparticles can cause the formation of a compact insulating layer on the SnO_2 surface, blocking the charge transport and extraction. Under careful concentration control, the optimal device achieved a optimal PCE of 23.83%, with significant improvements in V_{OC} and FF . The external quantum efficiency (EQE) measurement in Figure 5b determined the integrated J_{SC} values of the control and target devices, which were 23.97 and 24.17 mA cm^{-2} , respectively, coinciding with the results from the J - V test, which verifies the accuracy of the device current [31]. Figure 5c–f gives the statistical diagrams of V_{OC} , FF , PCE, and J_{SC} , respectively. These results indicate that Al_2O_3 -modified SnO_2 is capable of achieving an increased efficiency and good reproducibility.

Finally, the stability of unencapsulated F-PSCs based on different SnO_2 ETLs was evaluated under humidity and mechanical bending conditions, respectively. As shown in Figure 5g, the control device exhibited rapid degradation under ambient conditions with 30% relative humidity at room temperature, and the initial efficiency decreased to below 80% after 18 days. In contrast, the target device retained ca. 80% of the initial performance after 30 days. For the mechanical durability of F-PSCs, the control device began to degrade in the initial bending treatment at a bending circus of 4 mm and lost over 20% of its initial efficiency after 3000 bending cycles (Figure 5h). Encouragingly, the original efficiency of the target device was retained until 500 bending cycles, with the value remaining over 80% after 5000 cycles, illustrating the significantly improved mechanical robustness. With the Al_2O_3 decoration, the improved crystalline quality of perovskite films

and the strengthened interfacial adhesion at the SnO₂-perovskite interface contribute to the collective optimization effect on the device longevity.

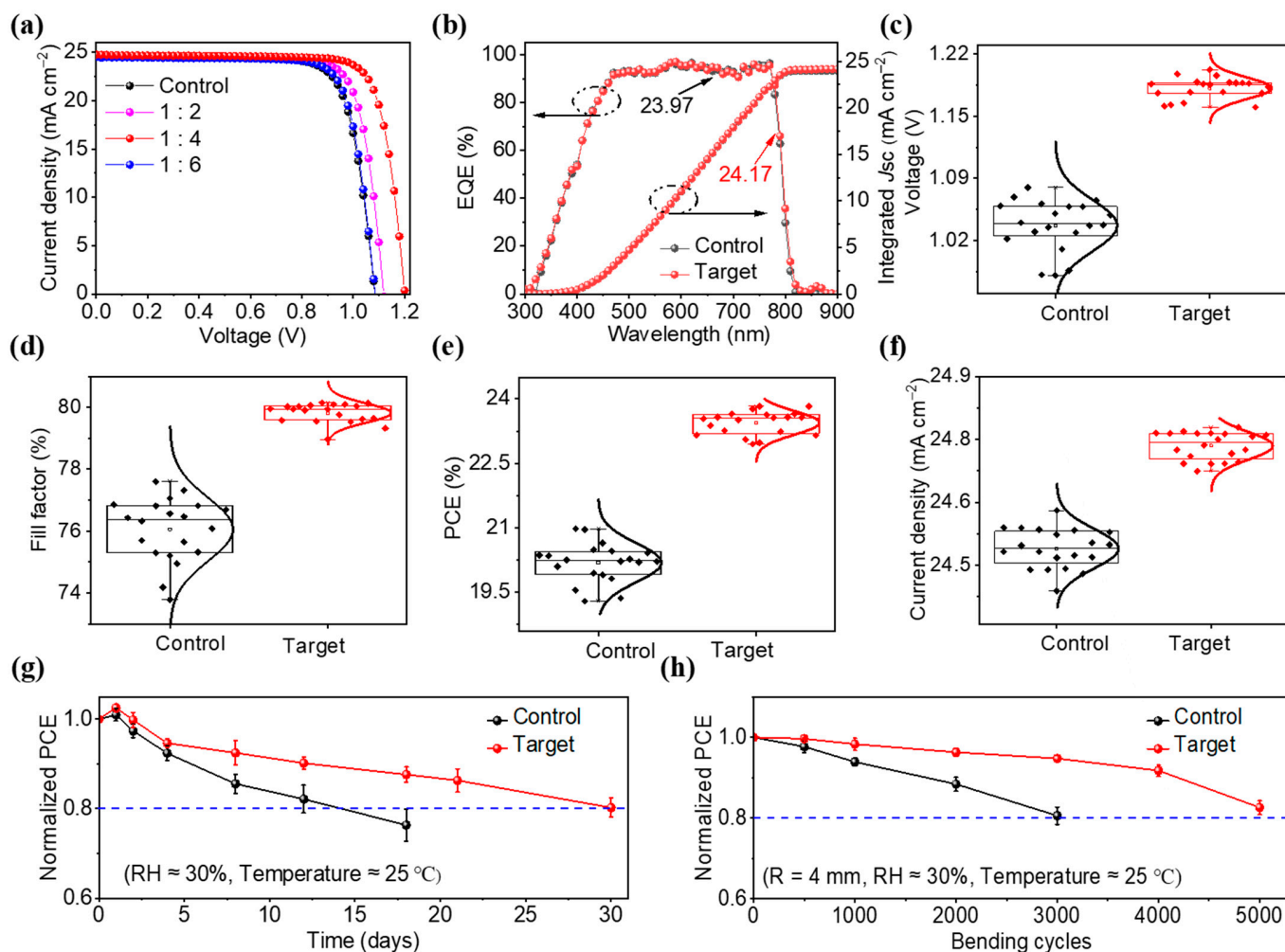


Figure 5. (a) J - V curves of the best-performing devices at different Al₂O₃ concentrations, (b) EQE curves and the corresponding integrated current density of the control and target devices. Statistical charts of (c) V_{OC} , (d) FF , (e) PCE , and (f) J_{SC} (20 devices for each condition), (g) the environmental stability, (h) bending cycle stability for control and target F-PSCs.

4. Conclusions

In this study, we proposed a novel media-filling strategy to smooth the buried interface of F-SPCs. The insulating Al₂O₃ nanoparticles were introduced at the perovskite-SnO₂ interface to fill the grooves on the SnO₂ surface and reduce its contact area with the absorber layer. The improved uniformity and roughness of the SnO₂ surface facilitate subsequent high-quality perovskite deposition with enlarged grain sizes and well-connected grain stacking. Our experimental results revealed that the addition of Al₂O₃ can effectively alleviate non-radiative recombination at the cathode interface through a synergistic effect on defect mitigation and charge extraction. As such, the optimized F-PSCs achieved a best-performing efficiency of 23.83%, which was higher than that of the control (20.98%). Moreover, the buried-interface smoothing can further enhance the mechanical durability of F-PSCs, which retained over 80% of the original efficiency after 5000 bending cycles. Our work illustrates the importance of buried interface management for the energy loss of F-PSCs, which may inspire further optimization research beyond molecular tailoring on the interfacial contact to realize the full device potential.

Supplementary Materials: The supporting information can be downloaded at: <https://www.mdpi.com/article/10.3390/en18010174/s1>, Figure S1: Tauc plots and calculated optical bandgap of SnO₂ and SnO₂/Al₂O₃ films. Figure S2: Schematic diagram of the device structure for SCLC method. Figure S3: Tauc plots and calculated optical bandgap for control and target perovskite films. Figure S4: Schematic diagram of the device structure. Table S1: Fitted parameters of the TRPL curves for SnO₂/perovskite and SnO₂/Al₂O₃/perovskite films. Table S2: Fitting parameters for electrochemical impedance spectra for SnO₂/perovskite and SnO₂/Al₂O₃/perovskite films. Table S3: Performance parameters of devices with different Al₂O₃ concentrations.

Author Contributions: E.Z. performed most of the experiments and wrote the draft. B.Y., L.Z. and D.L. contributed to the data analysis. Y.G. and T.N. designed the experiments and supervised the project. T.Y., C.L. and Y.Y. assisted in the preparation of films and devices. N.W. and C.T. helped with the J-V measurements. Z.Z. and W.D. helped optimize the schematic. Y.D. helped with manuscript discussion and analysis. All the authors revised the manuscript and contributed valuable suggestions. All authors have read and agreed to the published version of the manuscript.

Funding: The authors gratefully acknowledge the support of the Scientific Research Project of China Three Gorges Corporation (Project No. 202303014), which has significantly advanced research in perovskite photovoltaic technology and enabled key experimental investigations. We also express our sincere gratitude to the Scientific Research Project of China Three Gorges Corporation (Project No. 202103483) for its contribution to the development of perovskite photovoltaic technologies. Furthermore, we are thankful for the support of the Key R&D Programme of Zhejiang (Project No. 2022C01104) and the Key R&D Programme of Quzhou (Project No. 2021Z05), both of which have fostered innovation in high-efficiency perovskite photovoltaic applications and renewable energy technologies.

Data Availability Statement: The data presented in this study are available on request from the corresponding author.

Conflicts of Interest: Author Wanlei Dai, Buyi Yan and Lu Zhang were employed by the company Microquanta Semiconductor Co., Ltd. The remaining authors declare that the research was conducted in the absence of any commercial or financial relationships that could be construed as a potential conflict of interest.

References

1. ALee, G.; Kim, M.C.; Choi, Y.W.; Ahn, N.; Jang, J.; Yoon, J.; Kim, S.M.; Lee, J.G.; Kang, D.; Jung, H.S.; et al. Ultra-flexible perovskite solar cells with crumpling durability: Toward a wearable power source. *Energy Environ. Sci.* **2019**, *12*, 3182–3191.
2. Gao, Y.; Huang, K.; Long, C.; Ding, Y.; Chang, J.; Zhang, D.; Etgar, L.; Liu, M.; Zhang, J.; Yang, J. Flexible Perovskite Solar Cells: From Materials and Device Architectures to Applications. *ACS Energy Lett.* **2022**, *7*, 1412–1445. [[CrossRef](#)]
3. Huang, Z.; Li, L.; Wu, T.; Xue, T.; Sun, W.; Pan, Q.; Wang, H.; Xie, H.; Chi, J.; Han, T.; et al. Wearable perovskite solar cells by aligned liquid crystal elastomers. *Nat. Commun.* **2023**, *14*, 1204. [[CrossRef](#)] [[PubMed](#)]
4. Wu, Y.; Xu, G.; Xi, J.; Shen, Y.; Wu, X.; Tang, X.; Ding, J.; Yang, H.; Cheng, Q.; Chen, Z.; et al. In situ crosslinking-assisted perovskite grain growth for mechanically robust flexible perovskite solar cells with 23.4% efficiency. *Joule* **2023**, *7*, 398–415. [[CrossRef](#)]
5. Han, T.-H.; Zhao, Y.; Yoon, J.; Woo, J.Y.; Cho, E.-H.; Kim, W.D.; Lee, C.; Lee, J.-W.; Choi, J.-M.; Han, J.; et al. Spontaneous Hybrid Cross-Linked Network Induced by Multifunctional Copolymer toward Mechanically Resilient Perovskite Solar Cells. *Adv. Funct. Mater.* **2022**, *32*, 2207142. [[CrossRef](#)]
6. Li, M.; Zuo, W.-W.; Ricciardulli, A.G.; Yang, Y.-G.; Liu, Y.-H.; Wang, Q.; Wang, K.-L.; Li, G.-X.; Saliba, M.; Di Girolamo, D.; et al. Embedded Nickel-Mesh Transparent Electrodes for Highly Efficient and Mechanically Stable Flexible Perovskite Photovoltaics: Toward a Portable Mobile Energy Source. *Adv. Mater.* **2020**, *32*, 2003422. [[CrossRef](#)] [[PubMed](#)]
7. Chen, C.H.; Su, Z.H.; Lou, Y.H.; Yu, Y.J.; Wang, K.L.; Liu, G.L.; Shi, Y.R.; Chen, J.; Cao, J.J.; Zhang, L.; et al. Full-Dimensional Grain Boundary Stress Release for Flexible Perovskite Indoor Photovoltaics. *Adv. Mater.* **2022**, *34*, 2200320. [[CrossRef](#)]
8. Zhu, X.; Xu, J.; Cen, H.; Wu, Z.; Dong, H.; Xi, J. Perspectives for the conversion of perovskite indoor photovoltaics into IoT reality. *Nanoscale* **2023**, *15*, 5167–5180. [[CrossRef](#)] [[PubMed](#)]
9. Liu, C.; Yang, T.; Cai, W.; Wang, Y.; Chen, X.; Wang, S.; Huang, W.; Du, Y.; Wu, N.; Wang, Z.; et al. Flexible Indoor Perovskite Solar Cells by In Situ Bottom-Up Crystallization Modulation and Interfacial Passivation. *Adv. Mater.* **2024**, *36*, 2311562. [[CrossRef](#)] [[PubMed](#)]

10. Chen, X.; Cai, W.; Niu, T.; Wang, H.; Liu, C.; Zhang, Z.; Du, Y.; Wang, S.; Cao, Y.; Liu, P.; et al. Crystallization control via ligand–perovskite coordination for high-performance flexible perovskite solar cells. *Energy Environ. Sci.* **2024**, *17*, 6256–6267. [[CrossRef](#)]
11. Tong, X.; Xie, L.; Li, J.; Pu, Z.; Du, S.; Yang, M.; Gao, Y.; He, M.; Wu, S.; Mai, Y.; et al. Large Orientation Angle Buried Substrate Enables Efficient Flexible Perovskite Solar Cells and Modules. *Adv. Mater.* **2024**, *36*, 2407032. [[CrossRef](#)] [[PubMed](#)]
12. Lan, Y.; Wang, Y.; Lai, Y.; Cai, Z.; Tao, M.; Wang, Y.; Li, M.; Dong, X.; Song, Y. Thermally driven self-healing efficient flexible perovskite solar cells. *Nano Energy* **2022**, *100*, 107523. [[CrossRef](#)]
13. Liu, J.; Zhao, Z.; Qian, J.; Liang, Z.; Wu, C.; Wang, K.; Liu, S.; Yang, D. Thermal Radiation Annealing for Overcoming Processing Temperature Limitation of Flexible Perovskite Solar Cells. *Adv. Mater.* **2024**, *36*, 2401236. [[CrossRef](#)] [[PubMed](#)]
14. Wu, X.; Xu, G.; Yang, F.; Chen, W.; Yang, H.; Shen, Y.; Wu, Y.; Chen, H.; Xi, J.; Tang, X.; et al. Realizing 23.9% Flexible Perovskite Solar Cells via Alleviating the Residual Strain Induced by Delayed Heat Transfer. *ACS Energy Lett.* **2023**, *8*, 3750–3759. [[CrossRef](#)]
15. Wang, Y.; Meng, Y.; Liu, C.; Cao, R.; Han, B.; Xie, L.; Tian, R.; Lu, X.; Song, Z.; Li, J.; et al. Utilizing electrostatic dynamic bonds in zwitterion elastomer for self-curing of flexible perovskite solar cells. *Joule* **2024**, *8*, 1120–1141. [[CrossRef](#)]
16. Yang, L.; Feng, J.; Liu, Z.; Duan, Y.; Zhan, S.; Yang, S.; He, K.; Li, Y.; Zhou, Y.; Yuan, N.; et al. Record-Efficiency Flexible Perovskite Solar Cells Enabled by Multifunctional Organic Ions Interface Passivation. *Adv. Mater.* **2022**, *34*, 2201681. [[CrossRef](#)] [[PubMed](#)]
17. Li, Z.; Jia, C.; Wan, Z.; Xue, J.; Cao, J.; Zhang, M.; Li, C.; Shen, J.; Zhang, C.; Li, Z. Hyperbranched polymer functionalized flexible perovskite solar cells with mechanical robustness and reduced lead leakage. *Nat Commun.* **2023**, *14*, 6451. [[CrossRef](#)] [[PubMed](#)]
18. Cai, W.; Yang, T.; Liu, C.; Wang, Y.; Wang, S.; Du, Y.; Wu, N.; Huang, W.; Wang, S.; Wang, Z.; et al. Interfacial Engineering for Efficient Low-Temperature Flexible Perovskite Solar Cells. *Angew. Chem. Int. Ed.* **2023**, *62*, e202309398. [[CrossRef](#)] [[PubMed](#)]
19. Hu, M.; Zhang, L.; She, S.; Wu, J.; Zhou, X.; Li, X.; Wang, D.; Miao, J.; Mi, G.; Chen, H.; et al. Electron Transporting Bilayer of SnO₂ and TiO₂ Nanocolloid Enables Highly Efficient Planar Perovskite Solar Cells. *Sol. RRL* **2020**, *4*, 1900331. [[CrossRef](#)]
20. Xu, Z.; Lou, Q.; Chen, J.; Xu, X.; Luo, S.; Nie, Z.; Zhang, S.; Zhou, H. Synergetic Optimization of Upper and Lower Surfaces of the SnO₂ Electron Transport Layer for High-Performance n–i–p Perovskite Solar Cells. *ACS Appl. Mater. Interfaces* **2024**, *16*, 34377–34385. [[CrossRef](#)] [[PubMed](#)]
21. Luo, C.; Zheng, G.; Gao, F.; Wang, X.; Zhan, C.; Gao, X.; Zhao, Q. Engineering the buried interface in perovskite solar cells via lattice-matched electron transport layer. *Nat. Photonics* **2023**, *17*, 856–864. [[CrossRef](#)]
22. Kiy, M.; Losio, P.; Biaggio, I.; Koehler, M.; Tapponnier, A.; Günter, P. Observation of the Mott–Gurney law in tris (8-hydroxyquinoline) aluminum films. *Appl. Phys. Lett.* **2002**, *80*, 1198–1200. [[CrossRef](#)]
23. Wu, M.; Duan, Y.; Yang, L.; You, P.; Li, Z.; Wang, J.; Zhou, H.; Yang, S.; Xu, D.; Zou, H.; et al. Multifunctional Small Molecule as Buried Interface Passivator for Efficient Planar Perovskite Solar Cells. *Adv. Funct. Mater.* **2023**, *33*, 2300128. [[CrossRef](#)]
24. Ye, J.; Li, Y.; Medjahed, A.A.; Pouget, S.; Aldakov, D.; Liu, Y.; Reiss, P. Doped Bilayer Tin(IV) Oxide Electron Transport Layer for High Open-Circuit Voltage Planar Perovskite Solar Cells with Reduced Hysteresis. *Small* **2021**, *17*, 2005671. [[CrossRef](#)] [[PubMed](#)]
25. Zheng, B.; Zheng, W.; Jiang, Y.; Chen, S.; Li, D.; Ma, C.; Wang, X.; Huang, W.; Zhang, X.; Liu, H.; et al. WO₃–WS₂ Vertical Bilayer Heterostructures with High Photoluminescence Quantum Yield. *J. Am. Chem. Soc.* **2019**, *141*, 11754–11758. [[CrossRef](#)]
26. Wu, G.; Li, X.; Zhou, J.; Zhang, J.; Zhang, X.; Leng, X.; Wang, P.; Chen, M.; Zhang, D.; Zhao, K.; et al. Fine Multi-Phase Alignments in 2D Perovskite Solar Cells with Efficiency over 17% via Slow Post-Annealing. *Adv. Mater.* **2019**, *31*, 1903889. [[CrossRef](#)] [[PubMed](#)]
27. Cai, Y.; Cui, J.; Chen, M.; Zhang, M.; Han, Y.; Qian, F.; Zhao, H.; Yang, S.; Yang, Z.; Bian, H.; et al. Multifunctional Enhancement for Highly Stable and Efficient Perovskite Solar Cells. *Adv. Funct. Mater.* **2021**, *31*, 2005776. [[CrossRef](#)]
28. Chen, W.; Chen, H.; Xu, G.; Xue, R.; Wang, S.; Li, Y.; Li, Y. Precise Control of Crystal Growth for Highly Efficient CsPbI₂Br Perovskite Solar Cells. *Joule* **2019**, *3*, 191–204. [[CrossRef](#)]
29. Gu, X.; Xiang, W.; Tian, Q.; Liu, S. Rational Surface-Defect Control via Designed Passivation for High-Efficiency Inorganic Perovskite Solar Cells. *Angew. Chem. Int. Ed.* **2021**, *60*, 23164–23170. [[CrossRef](#)] [[PubMed](#)]
30. Li, Z.; Wu, M.; Yang, L.; Guo, K.; Duan, Y.; Li, Y.; He, K.; Xing, Y.; Zhang, Z.; Zhou, H.; et al. 24.64%-Efficiency MA-Free Perovskite Solar Cell with V_{OC} of 1.19 V Enabled by a Hinge-Type Fluorine-Rich Complex. *Adv. Funct. Mater.* **2023**, *33*, 2212606. [[CrossRef](#)]
31. Chang, X.; Fang, J.; Fan, Y.; Luo, T.; Su, H.; Zhang, Y.; Lu, J.; Tsetseris, L.; Anthopoulos, T.D.; Liu, S.; et al. Printable CsPbI₃ Perovskite Solar Cells with PCE of 19% via an Additive Strategy. *Adv. Mater.* **2020**, *32*, 2001243. [[CrossRef](#)]

Disclaimer/Publisher’s Note: The statements, opinions and data contained in all publications are solely those of the individual author(s) and contributor(s) and not of MDPI and/or the editor(s). MDPI and/or the editor(s) disclaim responsibility for any injury to people or property resulting from any ideas, methods, instructions or products referred to in the content.